

Recombinant Silk Fiber Properties Correlate to Prefibrillar Self-Assembly

Lingling Xu, Nathan Weatherbee-Martin, Xiang-Qin Liu,* and Jan K. Rainey*

Spider silks are desirable materials with mechanical properties superior to most synthetic materials coupled with biodegradability and biocompatibility. In order to replicate natural silk properties using recombinant spider silk proteins (spidroins) and wet-spinning methods, the focus to date has typically been on modifying protein sequence, protein size, and spinning conditions. Here, an alternative approach is demonstrated. Namely, using the same ≈ 57 kDa recombinant aciniform silk protein with a consistent wet-spinning protocol, fiber mechanical properties are shown to significantly differ as a function of the solvent used to dissolve the protein at high concentration (the “spinning dope” solution). A fluorinated acid/alcohol/water dope leads to drastic improvement in fibrillar extensibility and, correspondingly, toughness compared to fibers produced using a previously developed fluorinated alcohol/water dope. To understand the underlying cause for these mechanical differences, morphology and structure of the two classes of silk fiber are compared, with features tracing back to dope-state protein structuring and preassembly. Specifically, distinct classes of spidroin nanoparticles appear to form in each dope prior to fiber spinning and these preassembled states are, in turn, linked to fiber morphology, structure, and mechanical properties. Tailoring of dope-state spidroin nanoparticle assembly, thus, appears a promising strategy to modulate fibrillar silk properties.

1. Introduction

Spider aciniform (or wrapping) silk is a remarkable protein-based, fibrous material with exceptional mechanical properties. Of the six fibrillar silks produced by spiders, aciniform silk has a distinct combination of tensile strength and extensibility, making it the toughest of the silks^[1,2] and making it tougher than synthetic fibers such as Kevlar, polyester, and nylon.^[3] The best understood class of spider silk, major ampullate (MA, or dragline) silk, contrasts as the strongest of the silks,^[4] with a

lower extensibility and correspondingly lower toughness than aciniform silk.

Aciniform silk is predominately made up of a single protein: aciniform spidroin (AcSp1). AcSp1 from *Argiope trifasciata*, which is the focus of this study, is composed of at least 14 highly conserved 200 amino acid-long iterated repeats (termed “W” units, where W_n is a concatenated protein containing n identical W units) comprising $>95\%$ of the protein sequence.^[1] Unlike other spidroins, where short motifs tend to be correlated with strength and extensibility,^[5–7] AcSp1 has a relatively broad and heterogeneous amino acid composition, making the link between structure and function elusive.


A further significant difference in aciniform versus MA silk behavior is the fact that AcSp1 undergoes a structural transition between soluble and fibrous forms that is conceptually similar to MA silk,^[8–12] but leads to a distinct fibrous structuring. In the highly concentrated soluble “dope” state, AcSp1 is a modular structure composed of $\approx 50\%$ globular helical domains connected together by $\approx 50\%$ disordered

linkers.^[13] Upon fiber formation, Raman spectromicroscopy studies of native and recombinant aciniform silk fibers imply that the protein retains a similar proportion of disorder alongside a mixture of moderately oriented β -sheet ($\approx 30\%$) and α -helical ($\approx 24\%$) structuring.^[12–15] Contrasting to this, a recent solid-state nuclear magnetic resonance (NMR) spectroscopy study implied that Raman spectroscopy is overestimating the amount of β -sheet content in aciniform silk fibers, with only $\approx 15\%$ β -sheet content identified alongside 40–50% α -helical content.^[16] Between soluble and fibrous forms, many spidroins undergo a structural transition from α -helices to β -sheets.^[8,10,11] This transition is believed to be key in providing strength to silk fibers. However, the retention of significant—or, almost all, as solid-state NMR would imply^[16]— α -helical content in the aciniform silk fiber is distinct. Given the unique toughness of aciniform silk, this may be an essential structural feature contributing to its unique extensibility.

Beyond the size, sequence, and structuring of a given spidroin, the distinct mechanical properties of spider silks are known to rely on a combination of factors that occur within anatomically and functionally distinct silk glands including spidroin production, solubilization into the dope state, and assembly into silk.^[12,17–19] Following from these factors, it has

Dr. L. Xu, N. Weatherbee-Martin, Prof. X.-Q. Liu, Prof. J. K. Rainey
Department of Biochemistry & Molecular Biology
Dalhousie University
Halifax, Nova Scotia B3H 4R2, Canada
E-mail: paul.liu@dal.ca; jan.rainey@dal.ca

Prof. J. K. Rainey
Department of Chemistry
Dalhousie University
Halifax, Nova Scotia B3H 4R2, Canada

 The ORCID identification number(s) for the author(s) of this article can be found under <https://doi.org/10.1002/sml.201805294>.

DOI: 10.1002/sml.201805294

been argued that the difficulties seen in achieving similar mechanical properties for non-native silks to those of natural materials are due to incomplete identification of appropriate conditions to mimic the natural spinning processes of the spider.^[19] Of particular importance, two primary and perhaps not mutually exclusive mechanisms for spidroin structural transition during passage through the gland and duct have been advanced: a liquid crystalline hypothesis^[20] and a micellar hypothesis.^[21] Recently, cryoelectron microscopy and diffusion NMR experiments have provided evidence for nanoparticle self-assembly of spidroins in the gland setting, comprising micellar subdomains.^[22] In light of the requirement for self-assembly, phase transition, and anisotropic orientation inherent in these fibrillogenesis mechanisms, favoring of such a process in mimicking the natural silk assembly process is likely to be beneficial.

In vitro studies have shown that recombinant spidroins self-assemble and are stable as nanoparticles (generalizing from the micelle terminology of Jin and Kaplan^[21] to describe self-assembly of non-amphipathic species, with the caveat that spidroin micelles themselves may be likely to spontaneously self-associate to form larger nanoparticles in solution),^[22–24] including AcSp1 spidroins ranging in size from one to four concatenated W units, i.e., W_1 – W_4 .^[25,26] Fibrillar structures with a surface morphology of globular protrusions have been noted in both native spider silk^[27] and in recombinant aciniform silk.^[25] These findings are certainly qualitatively consistent with the hypothesis that self-assembly into micelles/nanoparticles in the spinning dope is an essential precursor for fiber formation. The resulting fibrillar morphology has, in turn, been noted to potentially profoundly influence mechanical behavior.^[27]

To date, the relation of protein self-assembly in the dope to fiber mechanical properties has not been a major focus of study. Previously, Arcidiacono et al. noted that spinning dope properties were highly important for protein assembly to facilitate fiber formation, but fiber mechanical properties were not directly correlated to dope behavior.^[28] More recently, Heidebrecht et al. compared fibers spun from a “classic spinning dope” versus a phase-separated “biomimetic spinning dope” and concluded that fibers produced from the classic spinning dope were stronger and tougher.^[29] This highlights the significance of spinning dope composition and the importance of protein preassembly before spinning, but a detailed mechanism was not described.

In short, most studies have focused on manipulating spidroin size, sequence, and spinning conditions, with the aim of improving the resulting silk fiber mechanical properties.^[28–44]

Direct comparison of spinning dope conditions, in turn allowing optimization of the resulting materials, has not been a major focus. We previously reported wet-spinning of fibers from a dope of W_3 dissolved in a 1,1,1,3,3,3-hexafluoro-2-propanol/ H_2O (HFIP/ H_2O) solvent mixture. Unfortunately, the resulting silk fibers exhibited a low extensibility and, correspondingly, low toughness.^[45] Here, we introduce a solvent mixture of trifluoroacetic acid/trifluoroethanol/ H_2O (TFA/TFE/ H_2O) also capable of solubilizing W_3 into a spinning dope and compare the resulting silk fiber ultrastructure, secondary structuring, and mechanical behavior, all of which are improved relative to fibers formed from the HFIP/ H_2O dope. With the goal of explaining the mechanism underlying these differences, the two spinning dopes were compared in detail, allowing us to trace the distinct fiber behavior and properties back to the protein structuring and nanoparticle assembly state in the spinning dope. This relationship between the self-assembly state in the dope to fiber properties provides an alternative parameter to tweak in the search for optimal artificial silk fiber formation conditions.

2. Results and Discussion

2.1. Silk Fiber Characterization

2.1.1. Mechanical Properties

A TFA/TFE/ H_2O solvent mixture (in a ratio of 3/1/1 v/v/v; denoted as TFA/TFE dope, herein) solubilizes W_3 instantly at a high concentration (10%, w/v). The resulting spinning dope is amenable to continuous wet-spinning of silk fibers (denoted TFA/TFE fibers herein) using the method we previously introduced with an HFIP/ H_2O (7/3 v/v)-based spinning dope (denoted as HFIP dope and fibers, as appropriate, herein).^[45] Strikingly, the strength, extensibility, toughness, and Young's modulus for the “as-spun” (AS) fibers collected by spooling of the W_3 silk directly following passage through a 95% ethanol coagulation bath were all dramatically improved relative to those of HFIP AS fibers (Table 1 and Figure 1).

Post-spin stretching of wet-spun silk fibers, including W_3 fibers spun from an HFIP/ H_2O spinning dope, generally improves the strength, extensibility, and toughness of the material.^[29–37,44,45] Consistent with this, post-spin stretched W_3 fibers (denoted PS fibers; stretched to 4× the original length in H_2O) produced from TFA/TFE spinning dope exhibited a similar strength to those formed from HFIP/ H_2O , but a 16-fold improvement in extensibility over the PS HFIP fibers

Table 1. Mechanical properties of W_3 AS and PS fibers produced from TFA/TFE dope and HFIP dope (average \pm standard deviation) in comparison to natural aciniform silk from *Argiope trifasciata*.

Fiber type	Strength [MPa]	Extensibility [%]	Toughness [MJ m ⁻³]	Young's modulus [GPa]	Diameter [μ m]	Number measured
TFA/TFE_AS	80 \pm 6	4.5 \pm 1.4	2 \pm 0.7	2.3 \pm 0.6	19 \pm 1	8
HFIP_AS ^[45]	36 \pm 12	3.1 \pm 1.0	0.5 \pm 0.2	1.4 \pm 0.8	23 \pm 1	15
TFA/TFE_PS	100 \pm 24	41 \pm 13	37 \pm 14	2.3 \pm 0.7	10 \pm 1	10
HFIP_PS ^[45]	92 \pm 8	2.6 \pm 0.6	1.3 \pm 0.3	4.5 \pm 0.5	9 \pm 1	12
Natural fiber ^[1]	687 \pm 56	86 \pm 3	376 \pm 39	\approx 10 \pm 4	0.35 \pm 0.01	Not given

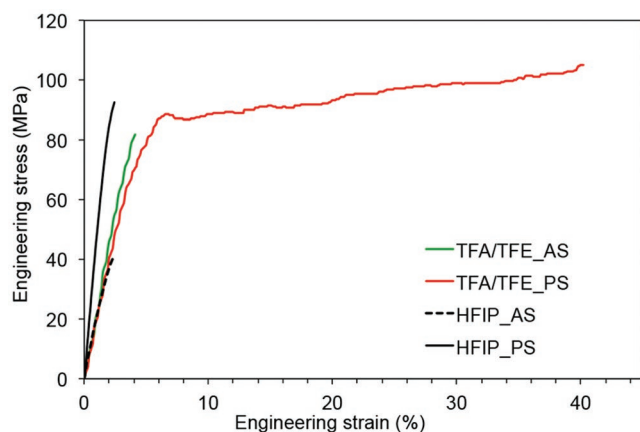


Figure 1. Representative stress–strain curves for AS and PS W_3 fibers produced from HFIP and TFA/TFE dopes (aggregate data are in Table 1).

(Table 1). As a result, PS TFA/TFE fibers exhibited a 28-fold increase in toughness (36.9 MJ m^{-3}) relative to PS HFIP fibers (1.3 MJ m^{-3}).

In wet-spinning of recombinant MA silk-based proteins from aqueous dopes, Arcidiacono et al. highlighted the importance of spinning dope properties as a function of protein construct to allow fiber formation.^[28] Particularly, preforming of β -sheet content in the dope prior to spinning was noted as a factor likely to be important in enhancing fiber formation. Heidebrecht et al. subsequently demonstrated that aqueous spinning dope solvent composition for wet-spinning of recombinant MA-based spidroins directly influenced the resulting fiber mechanical properties.^[29] Similar to Arcidiacono et al., the involvement of prestructuring in the dope was highlighted for improved fiber formation, with the functional role of nonrepetitive terminal domains in the MA protein constructs used being particularly emphasized. Although both of these studies implied the importance of silk protein prestructuring in the dope for fiber formation and properties, both employed aqueous spinning dopes with coagulation in alcohol/water baths. Other studies on recombinant spider silks have typically examined a single spinning dope (as reviewed, e.g., by Koepfel and Holland^[46]) and have tested the effects of downstream spinning parameters on fiber properties.

Given the context of other studies, it is thus surprising that wet-spinning of the same W_3 protein from two fluorinated alcohol/water-based spinning dopes—with all other spinning parameters remaining fixed—produces fibers with such a dramatic difference in extensibility. Notably, fluorinated alcohols are known to induce helicity.^[47,48] The previously noted potential importance of prestructuring of β -strands/sheets in the dope is hard to reconcile with these spinning dope conditions, assuming that this general behavior of fluorinated solvents holds true. Favoring of β -strand formation is also hard to rationalize with respect to the high degree of α -helical content retained in aciniform silk fibers according to Raman^[12,13,15] and NMR^[16] spectroscopy. In order to understand the mechanism by which mechanical differences in W_3 fibers are imparted at the dope stage, we next compare the two types of fibers for indications of the potential for protein prestructuring and self-assembly in the dope solution.

2.1.2. Surface Morphology

Fiber surface and internal morphology for W_3 AS and PS fibers were compared using field-effect scanning electron microscopy (FE-SEM; surface views in Figure 2, cross-sectional views of fractured fibers in Figure S1, Supporting Information) and atomic force microscopy (AFM; Figure S2 of the Supporting Information for PS fibers; AS fibers were poorly amenable to AFM). In all cases, SEM clearly demonstrates that the W_3 fibers are solid, rather than, e.g., tubular, in structure (Figure S1, Supporting Information). For TFA/TFE AS fibers, elongated globular structures are observed in fibrillar arrays ($\approx 0.6\text{--}1.2 \mu\text{m}$ wide) that align parallel to the long-axis on the fiber surface. HFIP AS fiber surfaces certainly exhibit globular structures, but without alignment to form a clear fibrillar surface morphology perpendicular to the long-axis at the sub- μm scale. Instead, multi- μm -scale fibrous units with grooves separating them (Figure 2, larger in scale in our previous study^[45]) are observed running parallel to the long-axis.

In comparison, naturally spun fibers are reported to have a smoother surface in comparison to recombinant silk fibers. The roughness of recombinant fibers may arise from the wet-spinning process, where the protein is extruded into a coagulation bath inducing solvent evaporation, dehydration, and fiber formation. The conditions of native aciniform silk fiber formation are still unknown, with a very distinct gland morphology from the much better characterized MA gland,^[12] but certainly would be expected to differ dramatically from wet-spinning from an organic solvent dope. This morphological difference may also be attributable to differences between the recombinant aciniform protein W_3 , comprising only 3 iterated repeats versus the native protein comprising at least 14 iterated repeats plus a C-terminal nonrepetitive domain and likely a N-terminal nonrepetitive domain. Additionally, the smoother surface morphology may more trivially arise from the fact that natural spun aciniform fibers at $\approx 0.35\text{--}0.5 \mu\text{m}$ ^[1,16,49] are much narrower than either AS recombinant silk fiber at $\approx 20 \mu\text{m}$. This difference in diameter may arise from the inner diameter of the spigot versus the syringe needle spinneret. Namely, the aciniform spigot from *Latrodectus hesperus* has a diameter of $\approx 0.5 \mu\text{m}$, consistent with its fiber diameter.^[49] The syringe needle used herein as the spinneret for wet-spinning, conversely, has an inner diameter of $127 \mu\text{m}$ while the AS fibers are $\approx 20 \mu\text{m}$ in diameter. The fact that many of the surface features observed in the AS recombinant silk fibers are on a similar size scale to the entire native fiber means that it is perhaps not surprising that native fibers appear smooth relative to the much larger AS fibers.

In both cases, the post-spin stretching process leads to fibers with a smoother surface morphology than the AS fibers. The sub- μm fibrillar structures become less apparent in TFA/TFE PS fibers, likely due to further fibrillar amalgamation and compression during post-spin stretching. It is also apparent that TFA/TFE PS fibers are smoother and more uniform than HFIP PS fibers, although the surfaces of PS fibers imaged by AFM also exhibit nanoparticle-like protein assemblies in both types of fibers (Figure S2, Supporting Information). Consistent with SEM results, average surface roughness determined from AFM image analysis shows that the HFIP PS fibers are rougher than

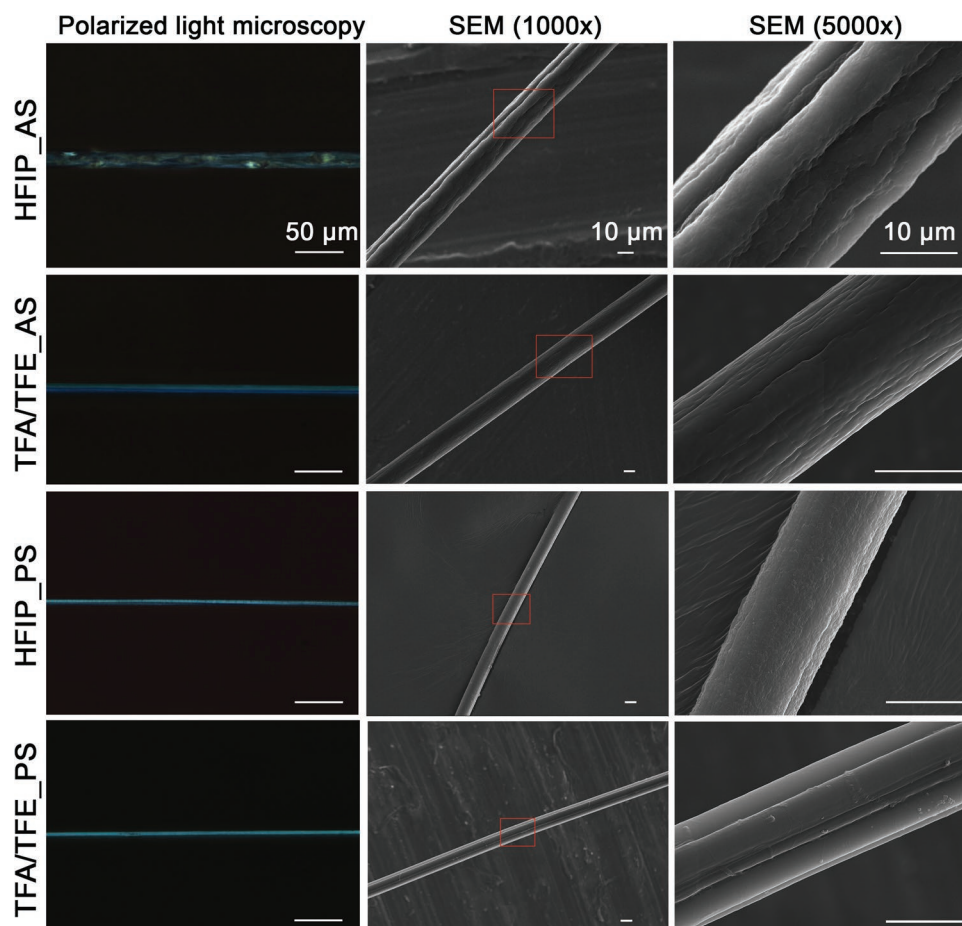


Figure 2. Representative polarized light microscopy and SEM micrographs of indicated W_3 fiber types.

TFA/TFE PS fibers (average roughness of 60 ± 8 nm versus 34 ± 10 nm for HFIP versus TFA/TFE fibers, respectively; more detailed comparison in Table S1, Supporting Information), with larger assemblies on the surface also consistent with SEM results.

The globular features observed in fibers formed from both spinning dopes are consistent with hierarchical assembly mediated by nanoparticle (e.g., the micellar species noted by Jin and Kaplan in silkworm fibroin^[21]) intermediates. It should be noted that we refer to these species as nanoparticles in the AcSp1 context, rather than micelles, as the W unit does not exhibit clear amphipathy, either at level of primary structure^[1] or tertiary structure,^[13] making the mechanism of self-assembly less clear-cut than for silkworm fibroin.^[26] The observed fibrillar species, in turn, appear to be formed by ellipsoidal elongation of nanoparticles in the post-spin stretching step. Similar fibril-bundle structuring has been observed in natural spider silks and collagen, with the resulting roughness and interfibrillar interactions postulated to provide crack-stopping functionality and important ramifications for the strength, extensibility, and toughness of the fiber in question.^[27,50–53] Therefore, the combination of improved nanoscale uniformity and fibrillar alignment observed in TFA/TFE versus HFIP PS fibers may play a role in the significant enhancement of mechanical properties that is observed.

2.1.3. Molecular Anisotropy

Considering individual hierarchically assembled units, the degree of molecular orientation and alignment relative to the fiber axis are also critical in determining the ultimate mechanical properties of fibers.^[15,53–56] To probe this phenomenon, polarized light microscopy was employed to characterize anisotropy by birefringence, permitting qualitative and correlative analysis of the overall degree of molecular orientation^[54,57,58] in each type of W_3 fiber (Figure 2). Notable differences can be observed between the two types of AS W_3 fibers. Namely, TFA/TFE AS fibers exhibit both a greater degree of birefringence and greater uniformity of this phenomenon relative to HFIP AS fibers. This is indicative of greater overall molecular orientation within TFA/TFE fibers, correlating to the greater fiber strength observed upon spinning from TFA/TFE versus HFIP.

Consistent with our previous observation of increased birefringence for PS versus AS fibers spun from HFIP dope^[45] (also clear in Figure 2), as well as with other recombinant silks,^[54,57] birefringence increased in TFA/TFE fibers following post-spin stretching (Figure 2). This is suggestive of post-spin stretching-induced improvements in molecular alignment, correlating well with the observed improvement in mechanical properties upon post-spin stretching in both cases. Despite this agreement, since birefringence is only sensitive to the degree

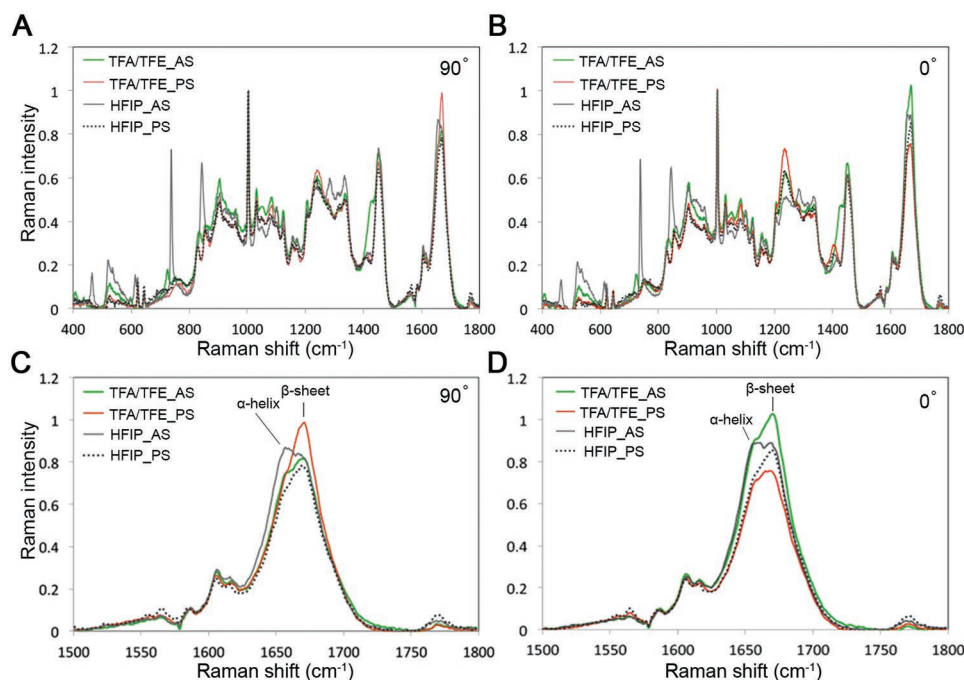


Figure 3. Representative Raman spectra of indicated W_3 fiber type with incident light polarized perpendicularly (90°) or parallel (0°) to fiber long-axis. A,B) Full spectra. C,D) Amide I bands enlargements.

of overall molecular orientation within the fibers, crystalline and amorphous regions within silk fibers cannot be directly distinguished.^[54,57–59] Given a general increase in anisotropy for fibers of improved mechanical properties, regardless of the spinning dope employed, we next sought to directly compare protein conformation and orientation in each type of fiber.

2.1.4. Secondary Structuring and Orientation

Raman spectromicroscopy was employed to analyze AS and PS W_3 fibers spun from the HFIP and TFA/TFE spinning dopes (Figure 3A,B). All spectra share common features arising from aromatic residues (for example Phe at ≈ 1003 and 1032 cm^{-1} and Tyr at 829 , 855 , and 1615 cm^{-1}), consistent with previous Raman spectromicroscopy studies of recombinant AcSp1 and native aciniform silks.^[12,13,15] There are some clear differences in amide I (Figure 3C,D) and amide III (Figure S3, Supporting Information) spectral regions, regardless of whether the incident laser light was polarized perpendicularly or parallel to the long-axis of the fiber. Because our experimental configuration does not allow for the selection of the polarization of both the incident beam and scattered Raman signal (only the incident beam is polarized, with the angle specified relative to the fiber long-axis), full spectral decomposition and orientational analysis are not possible.^[60] Despite these limitations, several key conclusions can still be drawn.

The amide I Raman band is mostly attributable to the C=O stretching vibration of peptide bonds. Since Raman scattering intensity is orientation dependent, variations in signal intensity may arise from i) differences in the number of scatterers at a given Raman transition and ii) the relative orientation of the

scattering unit. In the case of Raman scattering by an α -helix (amide I band at $\approx 1658\text{ cm}^{-1}$), higher intensity would correspond to increased α -helical content and/or to α -helices being oriented more parallel (for 0° polarization) or perpendicularly (for 90° polarization) relative to the fiber long axis. A higher β -sheet amide I Raman signal ($\approx 1671\text{ cm}^{-1}$) similarly could correspond to greater β -sheet content and/or to β -sheets being oriented more perpendicularly (for 0° polarization) or parallel (for 90° polarization) relative to the fiber long axis.

Based on the requirement that all Raman spectroscopic observations satisfy a consistent set of structurally based conclusions, qualitative comparisons were carried out (Table S2, Supporting Information). When comparing TFA/TFE PS to AS fibers, a depletion of α -helical structure occurred upon post-spin stretching, likely alongside conversion to β -sheet. Additionally, β -sheet alignment became more parallel with respect to the fiber long axis, in agreement with birefringence results (Figure 2). This conclusion is also supported by the characteristics of the observed Raman amide III signal (Figure S3, Supporting Information). Such post-spin stretching-induced structural conversion and alignment has also been observed in our previous studies employing W_3 in HFIP dope and with other protein fibers and is suggested to promote greater mechanical strength,^[15,32,45,57,61] coupling with the improved mechanical properties observed upon post-spin stretching.

Further insight comes from a direct comparison of AS and PS fibers produced from the two spinning dopes. In the case of AS W_3 fibers, those spun from TFA/TFE spinning dope exhibit a more pronounced β -sheet conformation than those from the HFIP spinning dope (Figure 3; Figure S2, Supporting Information), in line with the general correlation of β -sheet content to strength of silk fibers. Following post-spin stretching, the

β -sheet structural component became further enriched and aligned for both classes of fiber. Alignment relative to the fiber axis in TFA/TFE PS fibers was more pronounced, but a significantly increased strength was not noted for these fibers relative to HFIP fibers. Coupling with the high α -helical content in extensible native aciniform silk noted through solid-state NMR spectroscopy,^[16] the exceptional difference in extensibility may arise from a greater α -helical content for TFA/TFE fibers than HFIP fibers (Table S2, Supporting Information) providing spring-like behavior to facilitate extension as is proposed in α -helical coiled-coil-containing intermediate filaments.^[62] This likely couples with contributions from less ordered portions of the fiber, such as 3_1 -helical and turn content proposed to be important for dragline silk extensibility.^[63]

Coupling birefringence and Raman spectromicroscopy, both AS and PS W_3 fibers spun from the TFA/TFE spinning dope exhibited a greater degree of anisotropy at the molecular level and greater orientation of β -sheet structuring (Figures 2 and 3). These findings must also be considered in context of the hierarchical structural differences observed by SEM, where TFA/TFE fibers exhibited a smoother and more uniform fibrillar-like structure with aligned nanoscale globular domains. The improved mechanical properties, with respect to both extensibility and toughness for both AS and PS fibers produced from the TFA/TFE dope, can likely be attributed to all of the above factors. Given that the major distinction leading to these changes in properties for W_3 protein fibers was spinning dope composition, an understanding of the differences between the two spinning dopes was sought to explain these functional differences and to serve as a guide in screening of suitable solvents for other silk proteins.

2.2. Spinning Dope Comparison

2.2.1. Secondary Structure

W_3 protein secondary structuring in each dope solution was first evaluated by far-UV circular dichroism (CD) spectroscopy (Figure 4). The W_3 protein in the TFA/TFE spinning dope exhibited a positive band at ≈ 193 nm and negative bands at ≈ 208 and 222 nm consistent with significant α -helical content, as previously observed in 50×10^{-3} M potassium phosphate at pH 7.5,^[25] 20×10^{-3} M sodium acetate at pH 5.0,^[13] HFIP spinning dope,^[45] and native aciniform gland.^[12] This is also consistent with the typical α -helix stabilization behavior of fluorinated alcohol solvents,^[47,48] although the significant TFA content of the spinning dope is certainly a distinction relative to the fluorinated solvent/water mixtures that have been characterized in depth. As a whole, the α -helical structuring of aciniform spidroin in solution appears relatively insensitive to environment. The fact that W_3 protein solubilized in all of these conditions formed fibers exhibiting a structural conversion from α -helix to β -sheet suggests that α -helical structuring provides a stable aciniform spidroin form for storage in solution and a favorable starting point for structural transition^[13,64] under fiber-forming conditions.

Due to the relative insensitivity of CD spectroscopy, subtle conformation changes may not be reflected, as observed by

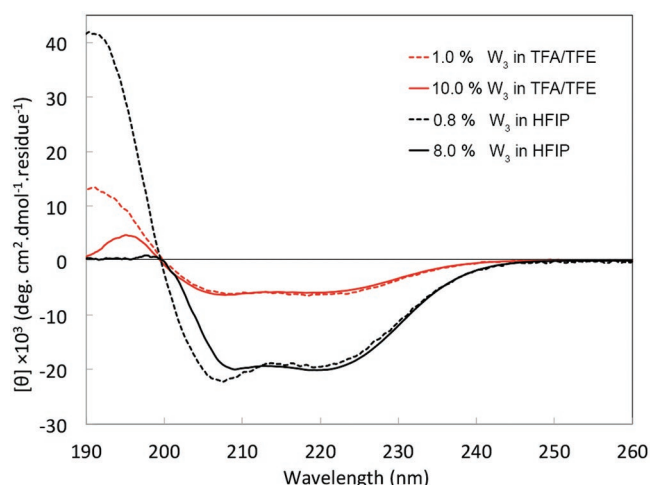


Figure 4. Far-UV CD spectra of W_3 in TFA/TFE dope (red dotted line: 1.0% and red solid line: 10.0%) and in HFIP dope (reproduced from previous study,^[45] black dotted line: 0.8% and black solid line: 8.0%).

our previous study using point mutations in recombinant aciniform spidroins.^[64] Therefore, quantitative structural deconvolution on the basis of CD spectral features was not performed. Instead, NMR spectroscopy was applied to examine W_3 secondary structuring in the two dopes.

In comparison to ^1H - ^{15}N correlation (heteronuclear single quantum coherence (HSQC)) NMR spectra for W_2 in acetate buffer, conditions from which fibers may be hand-drawn, ^1H - ^{15}N correlation (transverse relaxation optimized (TROSY))^[65] spectra of W_3 in each dope exhibit a similar degree of peak dispersion for backbone amide ^1H - ^{15}N spin-pairs (Figure 5). This is indicative of tertiary structuring being present in all situations. However, each condition gives rise to different peak patterns observable by ^1H - ^{15}N correlation spectroscopy. The distinct patterns observed in each environment may be attributable to: changes in the folded state of the globular core of the W unit; variation in the intrinsically disordered linker region(s) connecting W units; and/or,

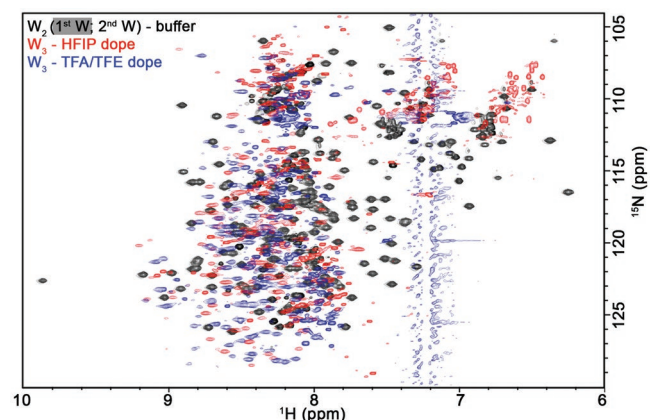


Figure 5. Overlay of ^1H - ^{15}N NMR correlation spectra of W_2 (HSQC: first W unit ^{15}N enriched and second W unit is natural abundance; grey: reproduced from previous study^[13]), W_3 in HFIP dope (TROSY: red) and in TFA/TFE dope (TROSY: blue).

changes in the solvent environment itself. Notably, the well-resolved ^1H – ^{15}N correlation spectra observed in each case are reflective of the monomeric W protein species population under a given condition, as higher-order assembly would attenuate the tumbling rate such as to preclude observation in this class of experiment^[66] (e.g., even a dimeric W_3 would be a ≈ 120 kDa species). Significant heteronuclear solution-state NMR signal intensity in each dope solution is, thus, suggestive of a high monomeric population. Dynamic light scattering (DLS) measurements also indicate a substantial population of monomeric species in both dopes (Figure S4, Supporting Information), with hydrodynamic diameter (d_{H}) estimated to be ≈ 7.7 – 10.5 nm. It should be noted that all DLS data analyses were based upon measured refractive indices (1.303 for HFIP and 1.311 for TFA/TFE samples, respectively) and viscosities (2.680 for HFIP and 2.926 mPa s for TFA/TFE samples, respectively). The d_{H} observed in both dopes is increased relative to the d_{H} of 6.3–7.3 nm previously inferred from pulsed field gradient diffusion NMR measurements and DLS of W_3 in 20×10^{-3} M sodium acetate buffer.^[13]

In comparing the NMR spectral behavior in each condition in more depth, W_3 in the HFIP dope exhibits a greater number of ^1H – ^{15}N resonances of varying intensity than either of the other conditions. This implies greater conformational heterogeneity of the W unit in this dope, relative to the other two conditions. This could arise from any or all of the following phenomena: i) an ensemble of distinct stable W_3 conformations being observed; ii) differences in W unit structuring within the context of W_3 ; and/or, iii) conformational exchange occurring at

a slow rate with respect to the NMR experimental timescale.^[67] At present, we cannot distinguish between these. In short, ^1H – ^{15}N correlation spectra are indicative of dope conditions providing significant monomeric populations with W_3 being structured in all cases but with evidence for greater conformational variability in the HFIP dope than in the TFA/TFE dope.

2.2.2. Protein Self-Assembly and Dope Viscosity

Despite the significant monomeric protein populations noted above, DLS signal correlation decay curves exhibit relatively long decay times with respect to the expectation for a homogeneously monomeric state (Figure 6A,B). This indicates that large diameter protein assemblies exist in each dope solution. Multicomponent decay is particularly apparent in HFIP dope, especially at longer correlation times corresponding to large species, indicating heterogeneity of large protein assemblies. The TFA/TFE dope, conversely, does not show apparent multicomponent decay, implying that large assemblies are more uniform in this condition. The heterogeneity in protein structure and dynamics noted in the monomeric form in the HFIP dope (Figure 5) may, in turn, be leading to this higher-order protein assembly heterogeneity.

To better characterize the nature of these self-assembled species, SEM was carried out on samples deposited on poly-D-lysine coated coverslips, demonstrating nanoparticles to be the primary species present (Figure 7). Interestingly, and unexpectedly, according to both SEM and DLS, not only did particle

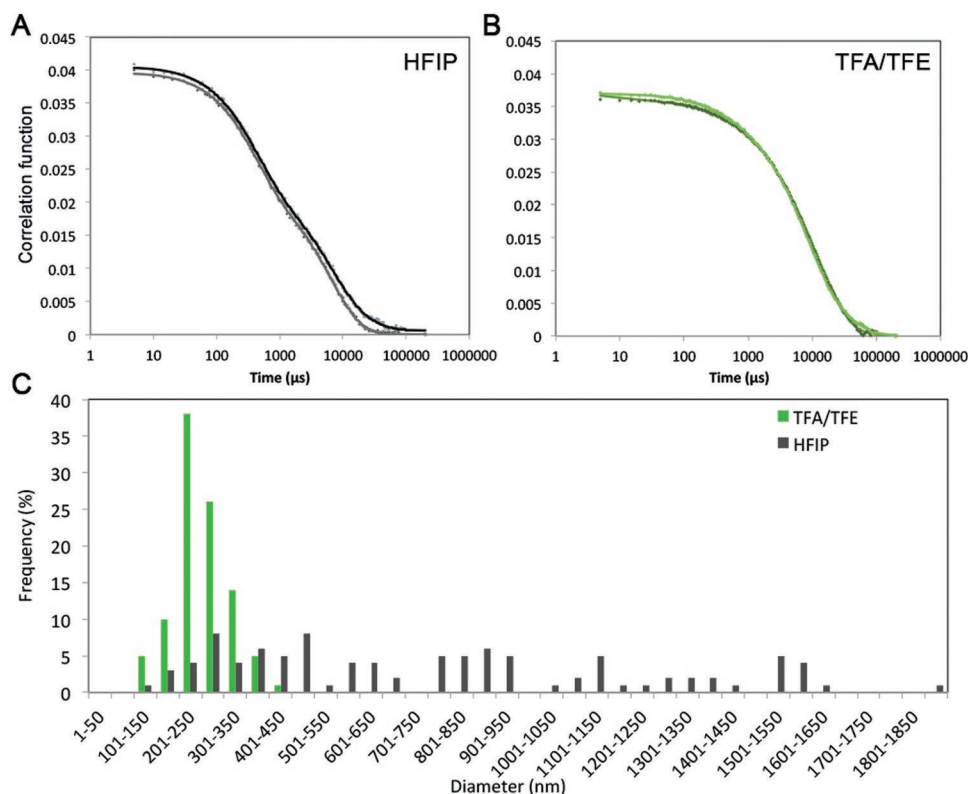


Figure 6. A,B) DLS signal correlation decays (symbols) and fits (lines) for A) HFIP and B) TFA/TFE dopes. C) Size distributions of nanoparticles formed in TFA/TFE dope (green; $n = 100$ particles) and HFIP dope (grey; $n = 100$ particles), based upon analysis of SEM micrographs.

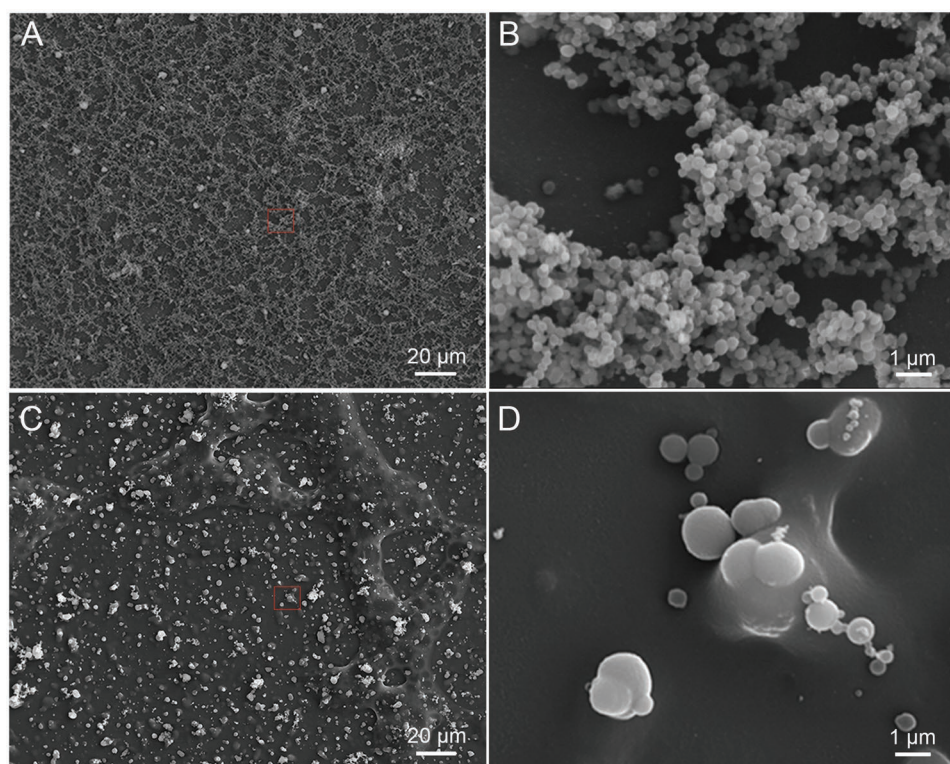


Figure 7. SEM micrographs of representative diluted A,B) TFA/TFE dope and C,D) HFIP dope samples. (B) and (D) are zooms of the boxed areas shown in (A) and (C), respectively.

homogeneity differ between dopes (as would be expected on the basis of DLS correlation functions), but particle size ranges also differed. Specifically, a much more uniform distribution of smaller (100–400 nm; predominantly 200–300 nm range) particles was observed in the TFA/TFE dope in contrast to a far wider distribution (100 nm to >2000 nm) in the HFIP dope (Figures 6C and 7). By SEM, the particles appear spherical in most cases, but instances of apparent fusion can be observed in both dopes. This phenomenon was more frequently seen in HFIP dope, implying that nanoparticles in HFIP solvent are more dynamic and less stable, consistent with the broader size distribution observed in HFIP dope. The observed morphologies, including the potential for nanoparticle fusion, are also consistent with the recent cryo-EM report of nanoparticle-like assemblies comprising multiple micellar species in the MA gland of *L. hesperus*.^[22]

Protein–protein interactions are also reflected in the observed viscosity of a given solution. A greater prevalence of protein–protein interactions would be expected to produce added friction and a more viscous dope. The viscosity of both HFIP and TFA/TFE dopes increased with increasing protein concentration, until a very sharp increase consistent with a gel-state (Table S3, Supporting Information). Before gelation, the W_3 TFA/TFE dope is more viscous than the HFIP dope at the same protein concentration, implying more friction between protein molecules and a greater propensity for protein–protein interactions. This may correspond to a more efficient self-assembly process for the more uniform nanoparticles observed in the TFA/TFE dope (i.e., a lower critical

concentration), in turn increasing viscosity more rapidly as a function of W_3 concentration.

2.3. Mechanism

We have found that recombinant aciniform spidroin W_3 can be solubilized at a relatively high concentration in two solvent mixtures producing dope solutions amenable to wet-spinning. In both conditions, the protein exhibited mainly α -helical structure, consistent with the state observed by Raman spectroscopy in the aciniform gland^[12] and with our high-resolution structural studies^[13] of W_1 and W_2 in aqueous solution at much lower concentration. Despite this similarity in secondary structuring, both ^1H – ^{15}N correlation NMR spectra and CD spectra exhibited clear differences between the two dopes, implying differences in folding and/or conformation of the helical domains and in the degree of conformational diversity observed between the two dopes. Echoing these differences in protein structural features and the relative number of distinct ^1H – ^{15}N backbone and side chain NMR spectral correlations observed, W_3 nanoparticles formed in the TFA/TFE dope were more uniform and smaller relative to those in the HFIP dope. This combination of variation in protein conformation and nanoparticle state is reflective of a distinct “prestructured” state in each spinning dope.

In fiber formation induced by shear force and dehydration, consistent with the micellar mechanism of silk fiber formation,^[21] the observed fibrillar morphology implies that

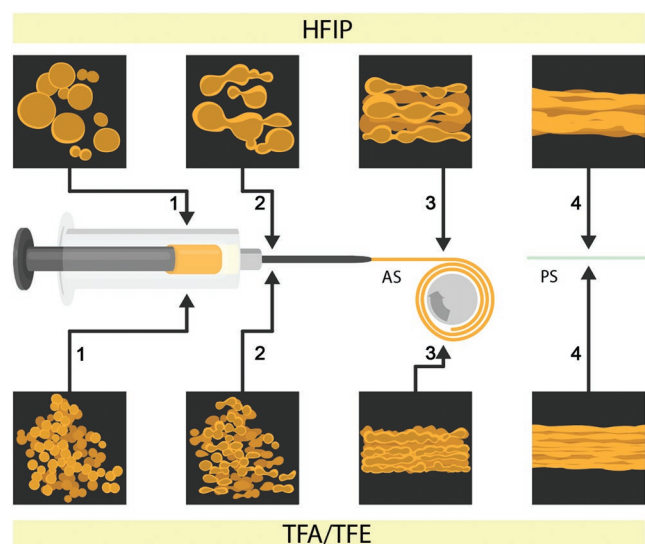


Figure 8. Recombinant aciniform silk wet-spinning fiber formation mechanism, with snapshots of four states of protein assembly (denoted 1–4) illustrated for each spinning dope. In state 1 (spinning dope), W_3 is preassembled into nanoparticles (TFA/TFE) or nano-microparticles (HFIP). In state 2 (spinneret), nanoparticles (or nanoparticles and microparticles) fuse together, due to shear forces exerted by the wet-spinning apparatus, likely with flow-induced alignment of assemblies. In state 3 (as spun (AS) fiber), fused assemblies become oriented and further fused in the fiber. In state 4 (post-spun stretched (PS) fiber), the fiber has increased homogeneity at molecular through ultrastructural levels.

preassembled nanoparticles (state 1, **Figure 8**) align and fuse together (state 2, **Figure 8**) through shear forces applied during constriction of the dope in the spinneret. This nanoparticle association and fusion stage may be coupled with a local increase in protein concentration through entropically driven solvent exclusion. Fused structures, in turn, orient and bundle together to form fibers (state 3, **Figure 8**). Concurrently, a structural transition occurs, from a highly α -helical solution-state (either in the spinning dope or the aciniform silk gland) to a mix of α -helical and β -sheet structuring in the fiber. The degree of particle fusion and alignment is then further enhanced through the post-spin stretching process for each class of fiber (state 4, **Figure 8**).

Correlating to the smaller and more uniform nanoparticles observed in the TFA/TFE dope than HFIP dope, the structural transition upon spinning from TFA/TFE was more efficient and the final fiber-state at levels from secondary structuring through to ultrastructural in both AS and PS states appeared more uniform. Correspondingly, the heterogeneous nanoparticle–microparticle state in the HFIP dope is reflected in the heterogeneity observed at molecular through ultrastructural levels. The less complete β -sheet conversion observed through ensemble-averaged measurement in AS fibers from HFIP dope relative to TFA/TFE dope may be envisioned as arising from two extreme situations: i) a situation where all proteins have relatively uniformly undergone a partial secondary structural transition; or ii) a situation where some W_3 proteins have undergone a complete transition while others have not. Our Raman spectromicroscopy measurements cannot distinguish between these cases, but it seems likely that the ultrastructural

and molecular heterogeneity would also persist at the level of secondary structural transition.

During the extrusion stage of the wet-spinning process upon entry to the spinneret, particles would be forced into contact, increasing likelihood of fusion and growth. The smaller and much more monodisperse nanoparticles observed in the TFA/TFE dope would be expected to pack together more optimally, with greater contact area and consistent connections between particles than the nonuniform particles in the HFIP dope (states 2 and 3, **Figure 8**). In the latter case, defects in packing would be expected; this, in turn, is consistent with the cavities and holes sometimes seen^[45] on the interior and surface of AS HFIP fibers. The influence of shear forces on the W_3 protein constituents of the larger particles in the HFIP dope would also be expected to be less pronounced, potentially contributing to the observation of a less complete structural conversion and consistent with situation (ii) noted in the previous paragraph where different W_3 molecules undergo differing degrees of structural conversion during the initial wet-spinning process.

3. Conclusion

In summary, inherent differences in protein prestructuring and self-assembly into a relatively homogeneous nanoparticle state or mixed nanoparticle–microparticle state in the solubilization stage prior to wet-spinning appear to directly influence the fibrous state. These differences lead to variation in the ultrastructure, the degree of molecular orientation, and the structural transitions induced within individual molecules. In turn, drastic differences in the mechanical properties of the resulting recombinant silk fibers are observed both immediately following wet-spinning into a coagulation bath and upon post-spin stretching treatment in water. Both spinning dopes exhibited similar viscosity increases as a function of protein concentration, albeit with differing rates of viscosity increase relative to protein concentration, and both also contain significant monomeric W_3 populations. As such, the success of wet-spinning from a given solvent seems most predictable through evaluation and optimization of protein self-assembly before spinning, with a specific target of an enriched homogeneous nanoparticle state being desirable both for maximal efficiency of nanoparticle packing and fusion to drive improved mechanical properties through optimal interaction between the resulting fused assemblies that pack together in the silk fiber.

4. Experimental Section

Protein Production and Purification: Following highly similar protocols to our prior His₆-SUMO- W_3 expression protocol,^[25] W_3 protein was produced in *Escherichia coli* BL21 (DE3) as His₆- W_3 and purified using nickel affinity gravity flow chromatography (Qiagen) under nondenaturing conditions following the conditions outlined by the manufacturer (Qiagen QIAexpressionist Handbook). After purification, the protein was dialyzed against water and lyophilized. Uniformly ¹⁵N-enriched W_3 was expressed in *E. coli* as a fusion protein, His₆-SUMO- W_3 following previous protein expression and purification procedures,^[25] with the exception that, before induction with IPTG, cells were transferred into M9 minimal medium and grown for an additional 30 min followed by induction. The M9 minimal medium was

supplemented with 1 g L⁻¹ ¹⁵NH₄SO₄ (Cambridge Isotope Laboratories, Andover, MA) and 2 g L⁻¹ D-glucose (at natural abundance) to provide uniform ¹⁵N-labeling. His₆-SUMO-tag proteolytic cleavage and protein purification were carried out as described previously.^[25]

Spinning Dope Preparation: Spinning dopes were prepared by suspending lyophilized W₃ protein (≈10%, w/v) in TFA/TFE/H₂O (3/1/1, v/v/v) or (≈8%, w/v) in HFIP/H₂O (7/3, v/v) in glass vials. TFA, TFE, and HFIP (≥99.0% (GC); grade: ReagentPlus) were obtained from Sigma-Aldrich (Oakville, ON) and type I deionized H₂O was used. The resulting suspensions were vortexed until homogeneous and incubated for 30 min at room temperature (22 ± 1 °C). After incubation, suspensions were centrifuged at 18 000 rcf for 30 min at 20 °C and the resulting supernatant was transferred into new glass vials.

Fiber Production and Characterization—Fiber Wet-Spinning and Post-Spin Stretching: A 100 µL Hamilton reversible needle (RN) syringe (Hamilton, Reno NV) attached to a needle (inner diameter, 0.127 mm) that serves as a spinneret was used to extrude spinning dope into coagulation bath (ethanol/water, 95/5) pushed by a syringe pump (KD Scientific KDS100, Holliston, MA) at a constant speed of 600 µL h⁻¹. Fibers were carefully picked up using tweezers from the coagulation bath and guided onto a 50 mL conical centrifuge tube (Fisher Scientific; Ottawa, ON) to collect.^[45] Post-spin stretching of AS fibers collected in this manner to 4× the original AS length was performed manually in deionized water using a home-built apparatus, as detailed previously.^[45]

Fiber Production and Characterization—Fiber Tensile Testing: Prior to mechanical testing, fibers were examined and diameters were determined, as previously described.^[45] Fibers were placed in the middle of a U-shaped paper frame (1 cm × 1 cm) with each end of fiber taped on the frame to create a 1 cm long fiber for mechanical testing. Right before mechanical testing, the side of paper frame between the two ends of fibers was cut to allow free stretching of fibers. Mechanical testing was performed at room temperature and ambient humidity (35% ± 5% RH) using a home-build mechanical testing set-up (similar to that of Huan et al.^[68]). Two stainless steel clamps were made (Department of Physics and Atmospheric Science Machine Shop, Dalhousie University) to grab each end of fibers to pull. One clamp was attached to a weight that was placed on an analytical balance (Mettler Toledo X5105DU, Greifensee, Switzerland) and the other clamp was attached to a syringe pump (KD Scientific, model 100 series, Holliston, MA) allowing for constant pulling of the fibers at a strain rate of 0.1 mm s⁻¹. The analytical balance was employed to monitor the weight change as a function of displacement of the syringe pump to determine the applied force, logged using instrument-specific software (LabX), and exported to Excel 2013 (Microsoft, Seattle, WA) for analysis. The data were processed in the same manner as described previously,^[45] but with an additional step added for calculation of both engineering strain and stress. Engineering strain values were obtained using the corresponding displacement values and dividing these values by the initial fiber length. For engineering stress, force (*F*) was calculated using Newton's second law of motion (*F* = *mg*, where *m* is weight loss measured by the balance as the fiber is pulled, and *g* is the acceleration due to gravity (9.81 m s⁻²)).

Fiber Production and Characterization—FE-SEM: Dope and fiber samples were observed using a S-4700 Cold Field Emission SEM (Hitachi, Toronto, ON). For dope samples, ≈30 µL aliquots of diluted (1/10) TFA/TFE and HFIP dope samples were deposited on glass coverslips, which had been coated with poly-D-lysine. Samples were allowed to sit at room temperature for ≈7 min to allow protein settling onto the surface before fixation. Samples were then critical point dried and coated with Au/Pd particles using a Low Vacuum Coater (EM ACE200, Leica Microsystems Inc., Richmond Hill, ON), as previously described.^[25] Fiber samples for surface and cross-sectional imaging were prepared in the same manner as before,^[45] using immersion in liquid nitrogen followed by breaking to generate ends representative of a cross-section of the fiber.

Fiber Production and Characterization—AFM: PS fibers were carefully placed on a glass slide (Fisher Scientific) coated with a thin layer of fresh LePage Epoxy glue (Henkel Canada Corporation, Mississauga,

ON). The fibers were left to sit at room temperature for at least 1 h to allow the glue to dry before imaging. AFM images were then acquired in intermittent-contact mode using a NanoWizard II Ultra (JPK, Berlin, Germany) mounted on an inverted optical microscope (Axio Observer A1, Carl Zeiss Canada, Toronto, ON) with silicon cantilevers having a resonance frequency of ≈300 kHz and a force constant of 40 N m⁻¹ (Tap 300-G, Budget Sensors, Sofia, Bulgaria). AFM micrographs were then processed with v3.3.32 NanoWizard IP software (JPK) and exported as TIFF files. Surface roughness values (average roughness, *R_a*; root mean square roughness, *R_q*; and peak-to-valley roughness, *R_t*) were determined based on height images, with six 2 × 2 µm² areas for each condition analyzed and averaged.

Fiber Production and Characterization—Polarized Optical Light Microscopy: Fibers were examined by polarized light microscopy using an Eclipse 600 microscope (Nikon Canada Inc., Mississauga, ON), equipped with cross polarizing filters and a quarter wave plate analyzer, with images being captured using an AmScope 10MP Microscope Digital Camera (Irvine, CA) and a Nikon TV lens C-0.45x.

Fiber Production and Characterization—Raman Spectromicroscopy: A diffraction-limited Raman scattering setup (modified from Gullekson et al.^[69]) consisted of an inverted optical microscope (1 × 71; Olympus, Center Valley, PA) coupled with an iHR550 Raman Spectrometer (Horiba Jobin Yvon, Edison, NJ) was employed and spectra were recorded at room temperature with 35 ± 5% humidity, as previously described.^[45] For a given condition, average values from three to four independent fibers were obtained at three to four different positions along the long axis of the fiber at either a perpendicular (90°) or parallel (0°) alignment relative to the incident polarized light. Fibers were routinely checked optically for structural deterioration from the laser to make sure no apparent damage occurred under these conditions.

Spinning Dope Characterization—CD Spectroscopy: Far-UV CD spectra of the neat spinning dope and a 1/10 dilution (1%) were recorded using a J-810 spectropolarimeter (Jasco, Easton, MD) at room temperature (22 ± 1 °C), as previously described.^[45] Three measurements were carried out per sample, averaged, blank subtracted, and converted to mean residue ellipticity.

Spinning Dope Characterization—NMR Spectroscopy: To prepare an HFIP NMR sample, lyophilized protein was solubilized in HFIP (deuterated)/H₂O (7/3, v/v) mixture to a final concentration ≈7% (w/v). The sample was kept at ≈20 °C for 3 days before NMR experiments. For TFA/TFE sample, lyophilized protein was solubilized in TFA/TFE (deuterated)/H₂O (3/1/1) at ≈20 °C for ≈1 h before NMR experiments. 2D ¹H–¹⁵N correlation experiments employing TROSY^[65] with sensitivity enhancement^[70] (Bruker pulse program troyetf3gpsi) were acquired at 30 °C using a 16.4 T Avance III spectrometer equipped with a 5.0 mm TCI cryoprobe (Bruker Canada, Milton, ON; 2048 × 256 points, 2.0 s recycle delay, 12 scans (HFIP/H₂O) or 8 scans (TFA/TFE/H₂O)). The data were processed and visualized using TopSpin 3.5. For comparative purposes, TROSY spectra were directly overlaid with previously published^[13] ¹H–¹⁵N HSQC spectra acquired in acetate buffer at 16.4 T and 30 °C for uniformly ¹⁵N/¹³C-enriched W₂ protein samples having one of each of the two W units segmentally labeled. The TROSY spectra acquired in fluorinated dope conditions were manually translated to the same chemical shift range as W₂ in buffer conditions; hence, chemical shifts in the dope conditions should not be considered absolute.

Spinning Dope Characterization—Viscometry and DLS: The viscosities of W₃ dopes at different concentrations (1, 5, 8, 10, and 12%) were measured following previously described^[45] protocols using a microviscometer (microVisc HVROC-L, RheoSense, San Ramon, CA) at 21 ± 1 °C. DLS measurements were performed using a BI-200SM Research Goniometer System (Brookhaven Instruments Corporation, Holtsville, NY) equipped with a Mini-L30 diode laser (637 nm, 30 mW intensity; Brookhaven Instruments Corporation). Dilutions (1/10) of TFA/TFE and HFIP dopes were incubated at 22 °C for 5 min prior to scattering measurement (in duplicate) at 60° angle for a total duration of 10 min at 22°C in a cylindrical quartz cell of 8 mm diameter and 74 mm height (Hellma Analytics, Plainview, NY). Refractive indices for each condition were measured for 25 µL drops (Refracto 30GS, Mettler-Toledo

AG, Schwerzenbach, Switzerland) following calibration with deionized water. Contin fitting was performed for DLS (Brookhaven Instruments DLS Software v. 5.89), employing the measured viscosity and refractive index for a given sample.

Supporting Information

Supporting Information is available from the Wiley Online Library or from the author.

Acknowledgements

L.X. and N.W.-M. contributed equally to this work. Thanks to Xiaoyi Ma for assistance in figure preparation; Dr. Laurent Kreplak for helpful discussions during development of the mechanical testing apparatus and for Raman spectromicroscope access; Dr. David Waisman for CD spectropolarimeter access; Dr. Michael Lee and Brandon Scott for polarized light microscope access; Ian Burton (National Research Council of Canada (NRC), Halifax NS) for NMR spectrometer support; and Bruce Stewart for technical assistance. The TCI probe for the 16.4 T NMR spectrometer at the NRC was provided by Dalhousie University through an Atlantic Canada Opportunities Agency Grant. This work was supported by Discovery Grants from the Natural Sciences and Engineering Research Council of Canada (NSERC, to X.-Q.L. and J.K.R.); a Discovery Accelerator Supplement (to J.K.R.); equipment and infrastructure Grants from NSERC (to J.K.R.), the Canadian Foundation for Innovation (to J.K.R.) and the Dalhousie Medical Research Foundation (to X.-Q.L. and J.K.R.); an NSERC Alexander Graham Bell Canada Graduate Scholarship (to N.W.-M.); and a Canadian Institutes of Health Research New Investigator Award (to J.K.R.)

Conflict of Interest

The authors declare no conflict of interest.

Keywords

fiber, nanoparticle, spider silk, spinning dope, wet-spinning

Received: December 12, 2018

Revised: January 18, 2019

Published online: February 13, 2019

- [1] C. Y. Hayashi, T. A. Blackledge, R. V. Lewis, *Mol. Biol. Evol.* **2004**, *21*, 1950.
- [2] R. C. Chaw, Y. Zhao, J. Wei, N. A. Ayoub, R. Allen, K. Atrush, C. Y. Hayashi, *BMC Evol. Biol.* **2014**, *14*, 31.
- [3] J. M. Gosline, P. A. Guerette, C. S. Ortlepp, K. N. Savage, *J. Exp. Biol.* **1999**, *202*, 3295.
- [4] T. A. Blackledge, C. Y. Hayashi, *J. Exp. Biol.* **2006**, *209*, 2452.
- [5] C. L. Craig, C. Riekel, *Comp. Biochem. Physiol., Part B: Biochem. Mol. Biol.* **2002**, *133*, 493.
- [6] C. Y. Hayashi, N. H. Shipley, R. V. Lewis, *Int. J. Biol. Macromol.* **1999**, *24*, 271.
- [7] J. D. van Beek, S. Hess, F. Vollrath, B. H. Meier, *Proc. Natl. Acad. Sci. USA* **2002**, *99*, 10266.
- [8] D. H. Hijirida, K. G. Do, C. Michal, S. Wong, D. Zax, L. W. Jelinski, *Biophys. J.* **1996**, *71*, 3442.
- [9] A. Simmons, E. Ray, L. W. Jelinski, *Macromolecules* **1994**, *27*, 5235.
- [10] T. Lefèvre, S. Boudreault, C. Cloutier, M. Pézolet, *Biomacromolecules* **2008**, *9*, 2399.
- [11] T. Lefèvre, M. E. Rousseau, M. Pézolet, *Biophys. J.* **2007**, *92*, 2885.
- [12] T. Lefèvre, S. Boudreault, C. Cloutier, M. Pézolet, *J. Mol. Biol.* **2011**, *405*, 238.
- [13] M. L. Tremblay, L. Xu, T. Lefèvre, M. Sarker, K. E. Orrell, J. Leclerc, Q. Meng, M. Pézolet, M. Auger, X. Q. Liu, J. K. Rainey, *Sci. Rep.* **2015**, *5*, 11502.
- [14] M. E. Rousseau, T. Lefèvre, M. Pézolet, *Biomacromolecules* **2009**, *10*, 2945.
- [15] L. Xu, T. Lefèvre, K. E. Orrell, Q. Meng, M. Auger, X. Q. Liu, J. K. Rainey, *Biomacromolecules* **2017**, *18*, 3678.
- [16] B. Addison, D. Onofrei, D. Stengel, B. Blass, B. Brennen, J. Ayon, G. P. Holland, *Chem. Commun.* **2018**, *54*, 10746.
- [17] M. Andersson, L. Holm, Y. Ridderstrale, J. Johansson, A. Rising, *Biomacromolecules* **2013**, *14*, 2945.
- [18] M. Andersson, G. Chen, M. Otikovs, M. Landreh, K. Nordling, N. Kronqvist, P. Westermark, H. Jorvall, S. Knight, Y. Ridderstrale, L. Holm, Q. Meng, K. Jaudzems, M. Chesler, J. Johansson, A. Rising, *PLoS Biol.* **2014**, *12*, e1001921.
- [19] A. Rising, J. Johansson, *Nat. Chem. Biol.* **2015**, *11*, 309.
- [20] F. Vollrath, D. P. Knight, *Nature* **2001**, *410*, 541.
- [21] H. J. Jin, D. L. Kaplan, *Nature* **2003**, *424*, 1057.
- [22] L. R. Parent, D. Onofrei, D. Xu, D. Stengel, J. D. Roehling, J. B. Addison, C. Forman, S. A. Amin, B. R. Cherry, J. L. Yarger, N. C. Gianneschi, G. P. Holland, *Proc. Natl. Acad. Sci. USA* **2018**, *115*, 11507.
- [23] U. K. Slotta, S. Rammensee, S. Gorb, T. Scheibel, *Angew. Chem., Int. Ed.* **2008**, *47*, 4592.
- [24] Z. Lin, W. Huang, J. Zhang, J. S. Fan, D. Yang, *Proc. Natl. Acad. Sci. USA* **2009**, *106*, 8906.
- [25] L. Xu, J. K. Rainey, Q. Meng, X. Q. Liu, *PLoS One* **2012**, *7*, e50227.
- [26] L. Xu, M. L. Tremblay, K. E. Orrell, J. Leclerc, Q. Meng, X. Q. Liu, J. K. Rainey, *FEBS Lett.* **2013**, *587*, 3273.
- [27] C. P. Brown, C. Harnagea, H. S. Gill, A. J. Price, E. Traversa, S. Licoccia, F. Rosei, *ACS Nano* **2012**, *6*, 1961.
- [28] S. Arcidiacono, C. M. Mello, M. Butler, E. Welsh, J. W. Soares, A. Allen, D. Ziegler, T. Laue, S. Chase, *Macromolecules* **2002**, *35*, 1262.
- [29] A. Heidebrecht, L. Eisoldt, J. Diehl, A. Schmidt, M. Geffers, G. Lang, T. Scheibel, *Adv. Mater.* **2015**, *27*, 2189.
- [30] S. L. Adrianos, F. Teule, M. B. Hinman, J. A. Jones, W. S. Weber, J. L. Yarger, R. V. Lewis, *Biomacromolecules* **2013**, *14*, 1751.
- [31] A. E. Albertson, F. Teule, W. Weber, J. L. Yarger, R. V. Lewis, *J. Mech. Behav. Biomed. Mater.* **2014**, *29*, 225.
- [32] B. An, M. B. Hinman, G. P. Holland, J. L. Yarger, R. V. Lewis, *Biomacromolecules* **2011**, *12*, 2375.
- [33] A. Lazaris, S. Arcidiacono, Y. Huang, J. F. Zhou, F. Duguay, N. Chretien, E. A. Welsh, J. W. Soares, C. N. Karatzas, *Science* **2002**, *295*, 472.
- [34] E. Gnesa, Y. Hsia, J. L. Yarger, W. Weber, J. Lin-Cereghino, G. Lin-Cereghino, S. Tang, K. Agari, C. Vierra, *Biomacromolecules* **2012**, *13*, 304.
- [35] J. A. Jones, T. I. Harris, C. L. Tucker, K. R. Berg, S. Y. Christy, B. A. Day, D. A. Gaztambide, N. J. Needham, A. L. Ruben, P. F. Oliveira, R. E. Decker, R. V. Lewis, *Biomacromolecules* **2015**, *16*, 1418.
- [36] F. Teule, B. Addison, A. R. Cooper, J. Ayon, R. W. Henning, C. J. Benmore, G. P. Holland, J. L. Yarger, R. V. Lewis, *Biopolymers* **2012**, *97*, 418.
- [37] X. X. Xia, Z. G. Qian, C. S. Ki, Y. H. Park, D. L. Kaplan, S. Y. Lee, *Proc. Natl. Acad. Sci. USA* **2010**, *107*, 14059.
- [38] G. Lang, S. Jokisch, T. Scheibel, *J. Visualized Exp.* **2013**, *75*, e50492.

- [39] J. S. Stephens, S. R. Fahnestock, R. S. Farmer, K. L. Kiick, D. B. Chase, J. F. Rabolt, *Biomacromolecules* **2005**, 6, 1405.
- [40] B. Zhu, W. Li, R. V. Lewis, C. U. Segre, R. Wang, *Biomacromolecules* **2015**, 16, 202.
- [41] Q. Yu, C. Sun, *J. Biomed. Mater. Res., Part A* **2015**, 103, 721.
- [42] S. Rammensee, U. Slotta, T. Scheibel, A. R. Bausch, *Proc. Natl. Acad. Sci. USA* **2008**, 105, 6590.
- [43] C. G. Copeland, B. E. Bell, C. D. Christensen, R. V. Lewis, *ACS Biomater. Sci. Eng.* **2015**, 1, 577.
- [44] Z. Lin, Q. Deng, X. Y. Liu, D. Yang, *Adv. Mater.* **2013**, 25, 1216.
- [45] N. Weatherbee-Martin, L. Xu, A. Hupe, L. Kreplak, D. S. Fudge, X. Q. Liu, J. K. Rainey, *Biomacromolecules* **2016**, 17, 2737.
- [46] A. Koepfel, C. Holland, *ACS Biomater. Sci. Eng.* **2017**, 3, 226.
- [47] F. D. Sonnichsen, J. E. Van Eyk, R. S. Hodges, B. D. Sykes, *Biochemistry* **1992**, 31, 8790.
- [48] A. Berkessel, J. A. Adrio, D. Huttenhain, J. M. Neudorfl, *J. Am. Chem. Soc.* **2006**, 128, 8421.
- [49] K. Vasanthavada, X. Hu, A. M. Falick, C. La Mattina, A. M. Moore, P. R. Jones, R. Yee, R. Reza, T. Tuton, C. Vierra, *J. Biol. Chem.* **2007**, 282, 35088.
- [50] G. Xu, L. Gong, Z. Yang, X. Y. Liu, *Soft Matter* **2014**, 10, 2116.
- [51] S. W. Cranford, *J. R. Soc., Interface* **2013**, 10, 20130148.
- [52] T. Giesa, M. Arslan, N. M. Pugno, M. J. Buehler, *Nano Lett.* **2011**, 11, 5038.
- [53] A. T. Nguyen, Q. L. Huang, Z. Yang, N. Lin, G. Xu, X. Y. Liu, *Small* **2015**, 11, 1039.
- [54] M. Sun, Y. Zhang, Y. Zhao, H. Shao, X. Hu, *J. Mater. Chem.* **2012**, 22, 18372.
- [55] N. Du, X. Y. Liu, J. Narayanan, L. Li, M. L. Lim, D. Li, *Biophys. J.* **2006**, 91, 4528.
- [56] T. Scheibel, *Microb. Cell Fact.* **2004**, 3, 14.
- [57] W. Wei, Y. Zhang, Y. Zhao, H. Shao, X. Hu, *Mater. Des.* **2012**, 36, 816.
- [58] M. Cronin-Golomb, A. R. Murphy, J. P. Mondia, D. L. Kaplan, F. G. Omenetto, *J. Polym. Sci., Part B: Polym. Phys.* **2012**, 50, 257.
- [59] I. C. Um, H. Kweon, K. G. Lee, D. W. Ihm, J. H. Lee, Y. H. Park, *Int. J. Biol. Macromol.* **2004**, 34, 89.
- [60] M. E. Rousseau, T. Lefèvre, L. Beaulieu, T. Asakura, M. Pézolet, *Biomacromolecules* **2004**, 5, 2247.
- [61] G. Bratzel, M. J. Buehler, *J. Mech. Behav. Biomed. Mater.* **2012**, 7, 30.
- [62] M. Guthold, W. Liu, E. A. Sparks, L. M. Jawerth, L. Peng, M. Falvo, R. Superfine, R. R. Hantgan, S. T. Lord, *Cell Biochem. Biophys.* **2007**, 49, 165.
- [63] J. M. Gosline, M. E. DeMont, M. W. Denny, *Endeavour* **1986**, 10, 37.
- [64] M. Sarker, K. E. Orrell, L. Xu, M. L. Tremblay, J. J. Bak, X. Q. Liu, J. K. Rainey, *Biochemistry* **2016**, 55, 3048.
- [65] K. Pervushin, R. Riek, G. Wider, K. Wuthrich, *Proc. Natl. Acad. Sci. USA* **1997**, 94, 12366.
- [66] Y. Jiang, C. G. Kalodimos, *J. Mol. Biol.* **2017**, 429, 2667.
- [67] J. K. Rainey, L. Fliegel, B. D. Sykes, *Biochem. Cell Biol.* **2006**, 84, 918.
- [68] Y. Q. S. Y. Huan, Y. J. Dai, Y. Q. Liu, T. Y. Wang, T. H. Zhang, M. H. Liu, *Exp. Tech.* **2016**, 40, 737.
- [69] C. Gullekson, L. Lucas, K. Hewitt, L. Kreplak, *Biophys. J.* **2011**, 100, 1837.
- [70] M. Czisch, R. Boelens, *J. Magn. Reson.* **1998**, 134, 158.